Chemical Science

ROYAL SOCIETY OF CHEMISTRY

EDGE ARTICLE

View Article Online
View Journal | View Issue

Cite this: *Chem. Sci.*, 2025, **16**, 18766

All publication charges for this article have been paid for by the Royal Society of Chemistry

Thermally responsive multistate fluorescence coupled with uniaxial negative thermal expansion in 1D lead halide hybrids

Gang Yang,[a] Wei Ye,[b] Yueqi Shen,[c] Dong-Sheng Shao,*[a] Jian-Lan Liu,[a] Zheng-Fang Tian,[d] Weihua Ning *[c] and Xiao-Ming Ren *[a]

Lead halide hybrids exhibit excellent optoelectronic properties, particularly in the development of high-performance solar cells and light-emitting diodes (LEDs). Increasing attention is being directed toward their thermal expansion behavior, as temperature-dependent bandgaps are crucial for solar cell and light emitting applications. Here, we report two new isomorphic one-dimensional (1D) lead halide hybrids, [XMePyr][PbX_3] (XMePyr$^+$ = 1-(2-haloethyl)-1-methylpyrrolidinium; X = Br (**1**) or Cl (**2**)), featuring rare hemidirected PbX_5 (X = Br or Cl) square pyramidal chains, a stereochemically active coordination geometry uncommon in this class of materials. Both compounds undergo isostructural phase transitions at 255 K (**1**) and 351 K (**2**), likely driven by the stereochemically active $6s^2$ lone pair electrons of Pb^{2+}. Remarkably, they exhibit uniaxial negative thermal expansion (NTE) along the chain direction, arising from transverse vibrations within the chains, representing the first such NTE mechanism identified in 1D lead halide hybrids. Additionally, the NTE is coupled with unique photophysical properties: **1** displays excitation-dependent dual emission, while **2** exhibits negative thermal quenching. Both **1** and **2** show reversible fluorescence switching associated with their phase transitions and NTE behavior. These results deepen our understanding of structure–property correlations in lead halide hybrids and offer insightful guidelines for designing multifunctional optoelectronic materials.

Received 17th July 2025
Accepted 8th September 2025

DOI: 10.1039/d5sc05322f

rsc.li/chemical-science

Introduction

Since Miyasaka and coworkers first reported $MAPbI_3$-based photovoltaic devices with 3.8% power conversion efficiency in 2009,[1] lead halide hybrid materials have rapidly emerged as a major research focus. These materials exhibit tunable zero- to three-dimensional (0D to 3D) crystal structures[2–7] that enable highly tailorable electronic properties[8,9] and engineerable optoelectronic functionalities.[9,10] This structural versatility facilitates diverse applications in photovoltaics,[11,12] lighting,[13,14] sensing (visible-light/X-rays),[15–17] anti-counterfeiting,[18] ferroelectrics/piezoelectrics,[19–21] and dielectric/resistive switching.[22–24]

For optoelectronic devices like solar cells and LEDs, the band gap and its temperature dependence of an optoelectronic material are critical properties. Consequently, thermal expansion behavior of lead halide hybrids is emerging as a growing area of research interest. Keshavarz *et al.* demonstrated that δ-$FAPbI_3$ exhibits two negative thermal expansion (NTE) regions: below 173 K ($\alpha \approx -1.3 \times 10^{-4}$ K^{-1} between 173 and 150 K) and below 54.5 K ($\alpha \approx -2.5 \times 10^{-4}$ K^{-1}, attributed to ferroelectric domain formation).[25] Separately, Paschoal *et al.* revealed uniaxial NTE in 3D hybrid $[(CH_3)_2NH_2]PbBr_3$ over a wide temperature range, caused by the thermally induced shrinkage of vertex-sharing $[Pb_2Br_9]^{5-}$ bi-octahedra along the NTE axis, and this mechanism differs from the typical "wine-rack" distortion in other hybrids.[26] Despite these advances, thermal expansion properties of these materials remain underexplored.

In lead halide hybrids, structural phase transitions—often driven by thermally activated order-disorder transformations of organic cations—underpin key functionalities like ferroelectricity, piezoelectricity, and dielectric/resistive switching. Critically, the stereochemically active $6s^2$ lone pair electrons of Pb^{2+} can induce significant distortions that influence structural motifs and phase transitions.[27,28] While these lone pairs are known to act synergistically with phase transitions in 3D hybrids,[26] their precise role warrants deeper investigation.

To address these gaps, we synthesized two isomorphic 1D lead halide hybrids, [XMePyr][PbX_3] (XMePyr$^+$ = 1-(2-haloethyl)-1-methylpyrrolidinium; X = Br (**1**) or Cl (**2**)). Their crystal

[a]*State Key Laboratory of Materials-Oriented Chemical Engineering, College of Chemistry and Molecular Engineering, Nanjing Tech University, Nanjing 211816, P. R. China. E-mail: shaods@njtech.edu.cn; xmren@njtech.edu.cn*

[b]*College of Chemistry Engineering, Nanjing Tech University, Nanjing 211816, P. R. China*

[c]*State Key Laboratory of Bioinspired Interfacial Materials Science, Institute of Functional Nano & Soft Materials (FUNSOM), Soochow University, Suzhou, 215123, P. R. China. E-mail: whning@suda.edu.cn*

[d]*Hubei Key Laboratory for Processing and Application of Catalytic Materials, Huanggang Normal University, Huanggang 438000, P. R. China*

structures feature Pb^{2+} ions with stereochemically active, hemidirected coordination environments—a rare configuration in lead halide hybrids—stemming from the asymmetric charge distribution induced by the $6s^2$ lone pair electrons. The PbX_5 (X = Br or Cl) square pyramids form edge-sharing 1D chains along the *a*-axis, where the stereochemical activity of $6s^2$ lone pair electrons in Pb^{2+} ions synergistically drives an isostructural phase transition. Remarkably, both **1** and **2** exhibit (i) uniaxial NTE along the chain direction, arising from transverse vibrational mode of the chain, (ii) distinct multistate photoluminescence behaviors, with **1** displaying excitation-wavelength-dependent dual emission and **2** showing negative thermal quenching, and (iii) a reversible fluorescence switching mechanism that is coupled to their phase transitions and uniaxial NTE.

Results and discussion

Crystals of both **1** and **2** were grown using a similar solution evaporation method. These crystals exhibit high chemical and phase purity, as confirmed by microanalysis and PXRD (Fig. S1).

Variable-temperature single-crystal XRD analysis reveals that both **1** and **2** undergo isostructural phase transitions (Table S1). Such a type of phase transition has been observed in lead halide hybrids,[29–31] and the two compounds are isomorphic to each other in their respective high-temperature phase (HTP) and low-temperature phase (LTP), with similar unit cell parameters and a change trend of the typical interatomic geometry parameters with temperature. For brevity, only the crystal structure of **1** is described in detail here, while the structural details of **2** are provided in the SI (Fig. S2 and S3).

Compound **1** crystallizes in the orthorhombic space group *Pnma* in both its HTP (320 K) and LTP (150 K). The asymmetric unit is identical in both phases, comprising a half Pb^{2+} ion (labeled Pb1), one and a half Br^- ions (denoted Br1 and Br2), and a half 1-(2-bromoethyl)-1-methylpyrrolidinium cation.

In the LTP, Pb1, and Br1 (inorganic component) and Br3, N1, and C1–C3 (organic component) occupy the Wyckoff 4c position with mirror plane symmetry, while other atoms reside in general positions (Fig. 1a). The cation exhibits mirror plane symmetry, and its bond lengths and angles are within expected ranges. The Pb^{2+} ion is coordinated to five Br^- ions to form square pyramidal geometry (Fig. 1b). Four Br2 ions form the basal plane of the pyramid with two distinct Pb–Br bond lengths (3.0175(6) Å and 3.0698(6) Å), while Br1 occupies the apical position with a shorter Pb–Br bond (2.7773(8) Å). These bond parameters are comparable to the values of the reported lead bromide hybrids.[32,33] Pb1 and Br1 are positioned on opposite sides of the pyramidal basal plane, with Pb1 displaced by 0.13 Å from this plane, indicating that the $6s^2$ lone pair electrons of Pb^{2+} ions induce a nonspherical charge distribution, resulting in stereochemical activity, and the Pb^{2+} ion adopts a hemidirected coordination sphere. While hemidirected geometries are widely observed in Pb(II)-coordination polymers,[34] however, to the best of our knowledge, they are relatively scarce in lead halide hybrids, particularly in lead bromide/iodide systems.

The $PbBr_5$ square pyramids are connected to one-dimensional chains *via* edge-sharing, with the chains extending along the *a*-axis, and the cations occupy the interchain spaces of the inorganic chains (Fig. 1c, d and S4). As shown in Fig. 1e and f, the interatomic distance *d*1, corresponding to that between Br3 in the cation and Br2 in the inorganic chain, is 3.36 Å, significantly shorter than the sum of the van der Waals radii for two bromine atoms (3.70 Å).[35] Similarly, the distances *d*2 and *d*3 measure 3.02 and 2.94 Å, respectively, both slightly below the van der Waals sum for bromine and hydrogen (3.05 Å).[35] These results demonstrate the presence of Br···Br and charge-assisted H···Br hydrogen-bonding interactions between the cation and inorganic chains.

In the HTP, the cation retains an ordered structure (Fig. S5), and its lengths and angles are comparable to the corresponding values in the LTP. In the $PbBr_5$ coordination square pyramid, the apical Pb–Br bond length is 2.79 Å, while the two distinct Pb–Br bond lengths at the basal plane of the pyramid measure 3.01 Å and 3.11 Å. The Pb1 atom is displaced by 0.132 Å from the basal plane. Compared to the LTP, the apical Pb–Br bond

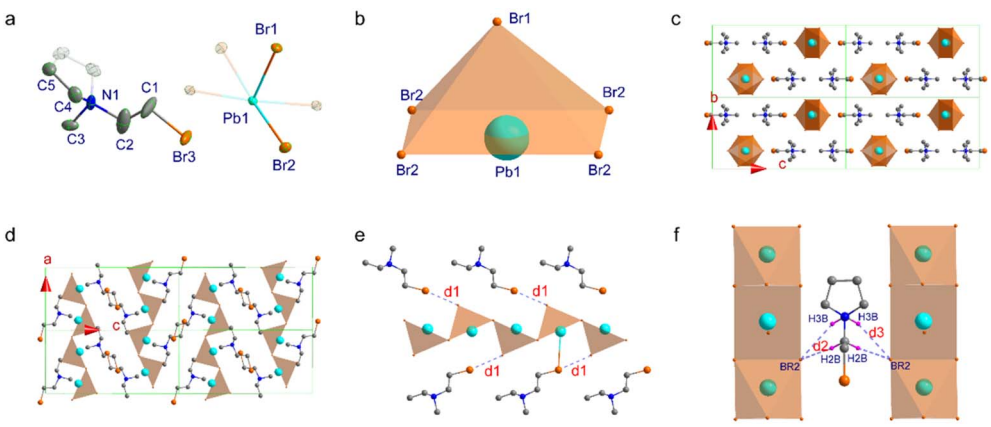

Fig. 1 Compound **1**: (a) ORTEP view; herein, the H-atoms are omitted for clarity and the ellipsoids are drawn at a 50% probability level for all non-H atoms. (b) The $[PbBr_5]^{3-}$ hemidirected square pyramid. (c and d) Packing diagrams viewed along the *a*- and *b*-axis, respectively. (e and f) Illustration of interatomic distances between inorganic chains and the cations, where *d*1, *d*2 and *d*3 represent the distances between Br3···Br1, H2b···Br2 and H3B···Br2, respectively.

elongates, whereas one basal Pb–Br bond lengthens and the other shortens. Notably, the dihedral angle of basal planes between adjacent $PbBr_5$ square pyramids increases significantly from 48.34° (LTP) to 50.95° (HTP). Additionally, the Br1···Br3 distance increases from 3.357 Å (LTP) to 3.398 Å (HTP). These changes in geometric parameters arise from the isostructural phase transition.

To further investigate the thermal behavior associated with this phase transition, we first examined the thermal stability of the compounds. Thermogravimetric (TG) analysis revealed that **1** remains stable up to 534 K, whereas **2** is thermally stable below 436 K, with its thermal decomposition temperature being significantly lower than that of **1** (Fig. S6). Based on their thermal stability, we explored their thermally induced phase transition characteristics using differential scanning calorimetry (DSC). The DSC plots reveal thermal anomalies for both **1** and **2** in sequence (Fig. 2a and b). During the heating process, compound **1** exhibits a broad endothermic event with the onset, peak and end temperatures at 229, 255 K and 279 K, respectively, while **2** shows an onset at 307 K, a peak temperature at 351 K and the end temperature at 395 K.

Notably, the phase transition temperatures of **1** and **2** differ by approximately 96 K despite only a halogen substitution (Br/Cl). To understand this difference, we performed Hirshfeld surface analysis at 150 K (where both compounds are in their LTP) and calculated their temperature-dependent Kitaigorodskii packing index (K.P.I.). The Hirshfeld surface analysis revealed no obvious differences in the intermolecular interactions between the cations and inorganic chains of **1** and **2** (Fig. S7). However, the K.P.I. analysis showed that **2** has consistently higher packing efficiency than **1** across the temperature range of 150–390 K. This indicates a higher packing density in **2** (Fig. S8), which we attribute to stronger intermolecular interactions between its cationic moieties and the inorganic chains. The increased energy barrier required for the phase transition in **2**, resulting from these stronger interactions, explains its higher T_C compared to **1**.

The enthalpy (ΔH) and entropy (ΔS) changes associated with the phase transitions were calculated from the DSC data, yielding $\Delta H = 0.864$ kJ mol^{-1} and $\Delta S = 3.390$ J mol^{-1} K^{-1} for **1** and $\Delta H = 0.942$ kJ mol^{-1} and $\Delta S = 2.686$ J mol^{-1} K^{-1} for **2**. The enthalpy and entropy of phase transitions are much lower than those in other 1D lead halide hybrids which underwent an order–disorder phase transition.[36–38] The small differences in both ΔH and ΔS align with the characteristics of an isostructural phase transition, which does not involve molecule rearrangement or an order–disorder transformation. It should be mentioned that the positions of the thermal anomaly peaks remain nearly unchanged during three consecutive heating–cooling cycles (Fig. S9), demonstrating the reversibility of the phase transitions for both compounds.

The temperature-dependent real part of dielectric permittivity (ε') measured during heating is plotted in Fig. S10. For **1**, the ε' values range from 14.8 to 17.6 across 120–360 K at selected frequencies between 1 kHz and 10 MHz. For **2**, the ε' values span from 18.2 to 39 over 250–423 K in the same frequency range (1 kHz–10 MHz). These values are comparable to those reported for other 1D lead halides.[39,40]

In the plots of ε' *vs.* T, a gradual knee-shaped transition occurs from the LTP to the HTP near 252 K for **1** and around 350 K for **2** (inset of Fig. S10b), and neither compound exhibits abrupt changes in dielectric permittivity during the phase transitions, indicating that both compounds possess quite similar crystal structures between the LTP and HTP. This is in agreement with the structure analysis of their LTP and HTP crystal phases, and the phase transitions between the LTP and HTP do not drive sharp dielectric variations in both compounds owing to a lack of significant reconfiguration (including displacement and disorder of ions).

To explore the thermal expansion behavior, we analyzed the temperature dependence of relative cell parameters (defined as $P(T)/P(150\ \mathrm{K})$), where $P(T)$ and P(150 K) represent the cell parameters (*a*-, *b*-, *c*-axes, and cell volume *V*) at temperature T and 150 K, respectively. Fig. 2c and d show the $P(T)$/P(150 K) *vs.*

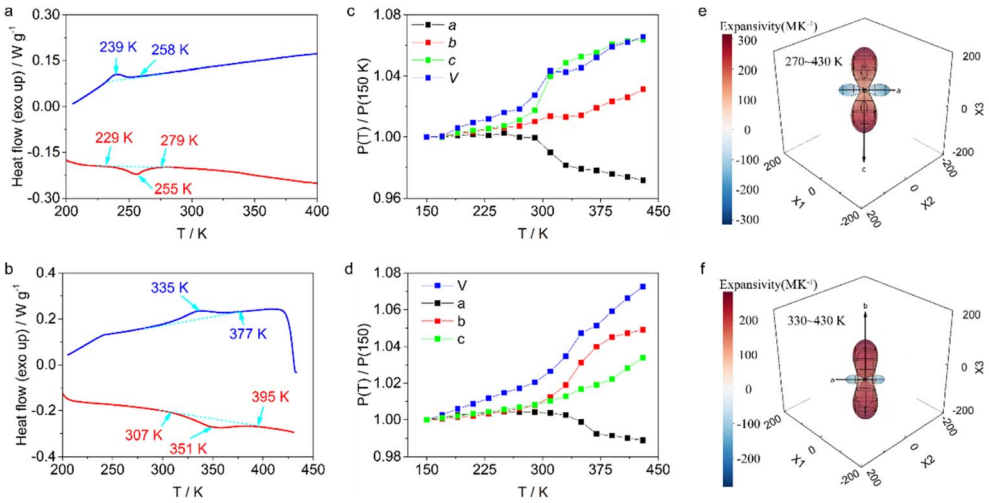

Fig. 2 DSC plots of (a) **1** and (b) **2**. Temperature dependence of relative cell parameters $P(T)/P(150\ \mathrm{K})$ in the 150–423 K range for **1** (c) and **2** (d). 3D distribution of the direction-dependent coefficients of thermal expansion (CTE) in the HTP for **1** (e) and **2** (f).

T plots for **1** and **2** over the 150–430 K range. Both compounds exhibit parallel trends in their temperature dependence of cell parameters, *i.e.*, the *b*-axis, *c*-axis, and volume *V* display positive thermal expansion (PTE) in both the LTP and HTP. In contrast, the *a*-axis shows zero thermal expansion (ZTE) in the LTP and NTE in the HTP. Notably, the maximum rate of change occurs at approximately 290 K for **1** and 370 K for **2**. These temperatures are slightly higher than the phase transition temperatures identified using the DSC peak maxima; they still fall within the broad onset-to-end temperature ranges for both compounds. Therefore, this discrepancy is understandable and consistent with the observed data.

The thermal principal axes (*X*1, *X*2, and *X*3) of **1** and **2** in both the LTP and HTP align with their crystallographic axes, as the crystals belong to the orthogonal system. In the LTP, the thermal principal axes (*X*1, *X*2, and *X*3) correspond sequentially to the *c*-, *a*-, and *b*-axes in **1** and *b*-, *c*-, and *a*-axes in **2**. The linear thermal expansion coefficients for *X*1–*X*3 are calculated as α_{X1} = +80(8) M K^{-1}, α_{X2} = +24(4) M K^{-1}, α_{X3} = +65(3) M K^{-1}, and volume CTE β = +170(11) M K^{-1} for **1** (150–250 K, LTP), compared to α_{X1} = +69(12) M K^{-1}, α_{X2} = +62(3) M K^{-1}, α_{X3} = +23(6) M K^{-1}, and β = +156(7) M K^{-1} for **2** (150–350 K, LTP).

In the HTP, the thermal principal axes (*X*1, *X*2, and *X*3) align sequentially with the *a*-, *b*-, and *c*-axes for **1** and *a*-, *c*-, and *b*-axes for **2**. The *a*-axis (*X*1-axis) exhibits NTE, with α_a = −188(19) M K^{-1} for **1** (270–423 K, HTP) *versus* α_a = −137(19) M K^{-1} for **2** (350–423 K, HTP). The *b*- and *c*-axes alongside *V* display a PTE effect, with α_b = +139(9) M K^{-1}, α_c = +315(47) M K^{-1}, and β = 273(25) M K^{-1} for **1** and α_b = +282(47) M K^{-1}, α_c = +201(13) M K^{-1}, and β = +351(22) M K^{-1} for **2**.

To visualize this anisotropy, three-dimensional (3D) distributions of the direction-dependent CTEs were generated for **1** and **2** in both the LTP and HTP using the PASCal software[41] and are illustrated in Fig. 2e, f and S11. Here, red, blue, and white regions represent PTE, NTE, and ZTE, respectively. To further understand the origin of this anisotropic thermal behavior, we analyzed the one-dimensional chain structures. Both **1** and **2** feature rigid 1D edge-sharing $\{[PbX_5]^{3-}\}_\infty$ square pyramidal chains along the *a*-axis. Discrete $XMePyr^+$ cations occupy the interchain spaces and interact with these inorganic chains *via* van der Waals forces. Both compounds exhibit uniaxial NTE along the *a*-axis. Consequently, the thermal expansion behavior parallel to the chains (*i.e.*, the *a*-axis) is governed by the rigid inorganic pyramidal chains. The key geometric parameters within these chains were analyzed, including the Pb–X bond lengths within the coordination pyramids, the distances of the Pb^{2+} ion and apical X^- ion to the basal plane of the coordination pyramid ($d(Pb^{2+})$ and $d(X^-)$), and the dihedral angle (θ) between the basal planes of adjacent coordination pyramids.

As shown in Fig. 3, S12 and S13, only the bond length of Pb–X2#1 (X = Br or Cl; the symmetric code #1 = −0.5 + *x*, 0.5 − *y*, 0.5 − *z*) exhibits PTE, the bond lengths of Pb–X1 and Pb–X2 (X = Br or Cl), as well as the distances of $d(Pb^{2+})$ and $d(X^-)$, show near ZTE, and the dihedral angle θ exhibits weak NTE in the LTP. Notably, the temperature dependence of Pb–X1, Pb–X2, and Pb–X2#1 bond lengths (X = Br or Cl) reverses in the HTP compared to the LTP.

Furthermore, the $d(Pb^{2+})$ switches from ZTE (in the LTP) to NTE (in the HTP), and the $d(X^-)$ transitions from ZTE (in the LTP) to PTE (in the HTP). The NTE of θ ($\theta = \pi$ − dihedral angle between the basic planes of two neighboring $PbBr_5$ square pyramids) is significantly stronger in the HTP than in the LTP. These results indicate that the uniaxial NTE along the a-axis in compounds **1** and **2** arises from transverse vibrational motion of the edge-sharing X^- ions within the two neighboring $PbBr_5$ square pyramids, perpendicular to the chain direction. Thereby, the isostructural phase transition in **1** and **2** can be ascribed to the temperature-dependent anharmonicity of this transverse vibration. Moreover, this type of vibrational mode is closely linked to the stereochemical activity of $6s^2$ lone pair electrons of Pb^{2+} ions. This mechanism is analogous to the thermal contraction observed in 2D graphene upon heating.[42,43] To the

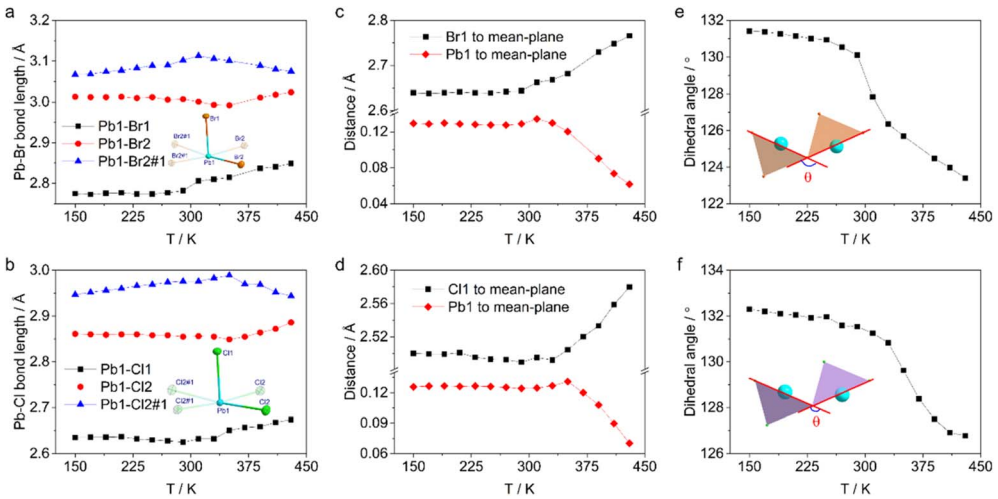

Fig. 3 Plots of Pb–X bond length *vs.* temperature within the range of 150–430 K for (a) $PbBr_5$ pyramid in **1** and (b) $PbCl_5$ pyramid in **2**. (c and d) Plots of distances of Pb1 and X1 (X = Br or Cl) to the basal plane of pyramids and (e and f) temperature-dependent θ angle between the basal planes of two neighboring coordination pyramids in **1** and **2**.

best of our knowledge, this represents the first example where transverse vibration within a 1D lead halide polyhedral chain induces NTE along its length in hybrid materials.

To further investigate their optical properties, solid-state UV-visible absorption spectra of **1** and **2** were recorded across the 200–800 nm spectral range under ambient conditions with corresponding Tauc curves displayed in the inset panels (Fig. 4a and S14a). The primary absorption bands appear in the 200–380 nm range for **1** and in the 200–330 nm range for **2**. These absorption features lie predominantly in the ultraviolet region, consistent with the colorless appearance of both hybrid compounds. The intense absorption bands are attributed to electron transitions from the valence band to the conduction band.

The optical band gap (E_g) was estimated from Tauc plots, yielding values of 3.12 eV for **1** and 3.62 eV for **2**. Electronic band structures (Fig. S15 and S16), total density of states (DOS), and partial density of states (PDOS) for C, Pb, and Br/Cl were calculated using DFT for both compounds. These calculations indicate indirect band gaps of E_g = 3.72 eV for **1** and E_g = 4.11 eV for **2**, which are higher than the corresponding optical band gaps. Band-edge absorption arises from charge-transfer transitions from X^- to Pb^{2+} centers coupled with Pb^{2+} 6s → 6p orbital transitions in both **1** and **2** (Fig. S15 and S16).

The excitation and emission spectra of **1** and **2** under ambient conditions are shown in Fig. 4b and S14b, respectively. Compound **1** exhibits two emission bands when excited by irradiation at 309 nm. The higher-energy emission band, centered at 403 nm, is relatively weaker compared to the lower-energy emission band, which peaks at 704 nm. These two bands can likely be attributed to band-edge and self-trapped exciton emission, respectively. The excitation spectrum of **1** reveals two peaks at 309 nm and 380 nm. Notably, the 380 nm peak aligns closely with the band-edge position observed in the absorption spectrum of **1** (Fig. 4a), further supporting the assignment of spectral bands in the emission spectrum.

The excitation and emission spectra of **2**, distinct from those of **1**, only show single bands (Fig. S14b). For **2**, the emission band peaks at 446 nm under 354 nm excitation and displays a broad half-peak width (~138 nm), which may be attributed to self-trapped exciton emission. The CIE coordinates are calculated to be (0.536, 0.395) for **1** and (0.213, 0.236) for **2**, corresponding to blue and orange light (Fig. S17), respectively. These values are consistent with the observed colors of the polycrystalline samples of **1** and **2** under ultraviolet light (λ = 254 and 365 nm), as shown in Fig. S18 and S19.

The excited-state lifetimes and fluorescence quantum yields of **1** and **2** were measured under ambient conditions. As shown in Fig. 4c and S14c, both compounds display characteristic fluorescence decay profiles. The excited-state lifetimes were obtained by fitting the decay curves with a two-exponential equation for **1** and a single-exponential equation for **2**, to give

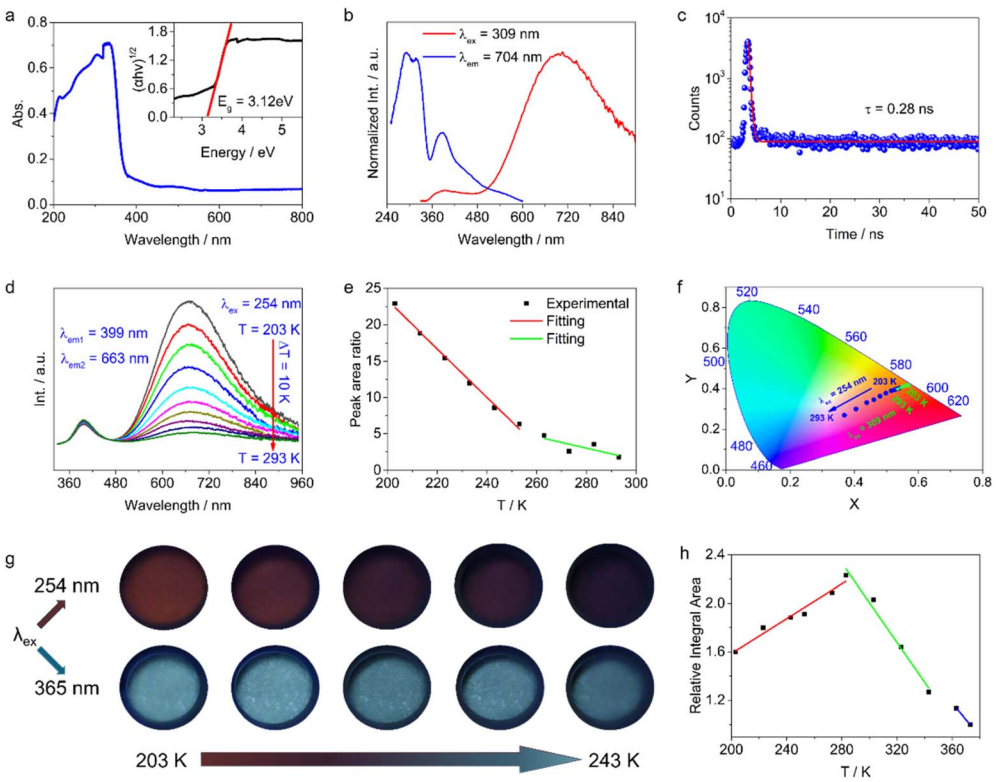

Fig. 4 UV-visible absorption spectra of (a) **1** under ambient conditions, and the inset of (a) shows the corresponding Tauc curve of **1**. Excitation and emission spectra of (b) **1**, and the emission decay curves of (c) **1** under ambient conditions. Variable temperature emission spectra in the 203–293 K range under excitation using 254 nm ultraviolet light (d), plots of the emission peak area ratio of the band at 663 nm to the band at 399 nm *versus* temperature (e), and the corresponding CIE chromaticity diagram (f) of **1**. (g) Photos of **1** under 254 and 365 nm ultraviolet light at different temperatures. A plot of emission peak area *vs.* temperature (h) for **2**.

the values of 0.28 ns for **1** and 1.01 ns for **2**. The fluorescence quantum yields were calculated to be 0.53% for **1** and 24.2% for **2**. The fluorescence quantum yields reported from typical zero- to three-dimensional (0D–3D) lead halide hybrids are summarized in Table S2. Compared with those, **2** shows higher fluorescence quantum yield in 1D lead halide hybrids. While an indirect bandgap semiconductor typically exhibits weak band-edge fluorescence, the presence of sub-bands in the excited state—such as a self-trapped state—can lead to self-trapped emissions with a higher quantum yield. This phenomenon has been observed in metal halide hybrids.[44]

Since compound **1** exhibits dual-band emission, its excitation wavelength-dependent fluorescence properties were further investigated. Fig. 4d and S20 show the emission spectra of **1** under 254 and 309 nm excitation over the temperature range 203–293 K, respectively. Under the ultraviolet light irradiation at 254 nm, **1** shows dual emission bands with the peak maximum at $\lambda_{em} = 399$ and 663 nm, respectively. As temperature increases, the emission intensity of the band centered at 399 nm remains nearly constant, while the intensity of the band peaking at 663 nm decreases significantly. The emission intensity at a given temperature (T) was quantified using either the maximum value or integrated area of a peak. The emission intensity ratio of the two bands, I_{663}/I_{399}, is plotted as a function of temperature, and is shown in Fig. 4e and S21, respectively. The peak area ratio of the band with the maximum at 663 nm to that at 399 nm decreases linearly within two distinct temperature ranges of 203–253 K and 263–293 K, each with a different slope (Fig. 4e and S21), exhibiting a feature of fluorescence switch. The turning point of two slopes between the temperature regime (253–263 K) is consistent with the critical temperature range of the structural phase transition, demonstrating the presence of coupling interaction between NTE and fluorescence switch. This change in emission intensity ratio results in an emission color shift from red to blue, exhibiting an obviously thermochromic effect (Fig. 4f and S22). The temperature-dependent CIE chromaticity coordinates agree well with the observed emission colors between 203 and 293 K (Fig. 4f). These phenomena are consistent with the observed colors of the polycrystalline samples of **1** under ultraviolet light ($\lambda = 254$ nm), as shown in Fig. 4g. Ratiometric luminescent materials show promise for temperature sensing[45,46] and gas detection.[47] In the LTP, the intensity ratio I_{663}/I_{399} of **1** varies linearly with temperature (adjusted $R^2 = 0.993$), indicating its potential for low-temperature sensing applications.

Under 309 nm light excitation, the variable-temperature emission spectra of **1** (203–293 K) are shown in Fig. S20. At 293 K, the emission maximum occurs at 704 nm, blue-shifting to 674 nm at 203 K, with intensity increasing upon cooling. Notably, the band-edge emission is quite weak under this excitation. In contrast to the pronounced thermochromism observed under 254 nm excitation, the emission color under 309 nm excitation shows little variation across the temperature range of 203–293 K (Fig. 4f).

Fig. S23 shows the emission spectra of **2** under 354 nm excitation across temperatures ranging from 203 to 373 K. The intensity of the emission band at ~446 nm increases between 203 and 283 K but decreases from 283 to 373 K as the temperature increases, exhibiting a non-monotonic thermal dependence. Strikingly, **2** displays thermally enhanced fluorescence in the 203–283 K range. Notably, the co-occurrence of thermally enhanced fluorescence and NTE features is exceptionally rare, not only in metal halide hybrids but across all known fluorescent materials.[48] We define the relative peak area and relative peak intensity as area(T)/area(373 K) and intensity(T)/intensity(373 K), respectively. These ratios are plotted as a function of temperature in Fig. 4h, which shows both decreasing rapidly above 283 K with increasing temperature. Notably, a distinct slope change occurs near the structural transition temperature ($T_C = 351$ K), suggesting that the emission process is coupled with NTE.

The thermal quenching and negative thermal quenching dual-emission behavior that occurred in **2** contrasts with conventional thermal quenching fluorescence, where elevated temperatures universally reduce intensity by amplifying molecular vibrations and enhancing thermal relaxation-driven non-radiative transitions, diverting excited-state energy to heat dissipation instead of photon emission, *i.e.*, thermal quenching. The enhancement of emission intensity with rising temperature is referred to as negative thermal quenching and the negative thermal quenching phenomenon is the characteristic of trapped state emission. In this situation, variable-temperature fluorescence involves two competing processes: thermal excitation of low-energy trapped states to high-energy radiative trapped states for the increasing emission intensity and the dissociation of the electron–hole pair with temperature for the decreasing emission intensity at high temperatures.[49]

The competition is described by the Shibata model,[50] wherein the emission intensity variation with temperature follows the relationship:

$$I(T) = \frac{I_0\left(1 + A\cdot\exp\left(-\frac{E_{a_1}}{k_B T}\right)\right)}{1 + B\cdot\exp\left(-\frac{E_{a_2}}{k_B T}\right)} \quad (1)$$

In eqn (1), I_0 denotes the fluorescence intensity at low temperature, the symbols A and B represent the probability factors, and E_{a1} and E_{a2} signify the activation energy for thermal excitation to high-energy trapped states and the dissociation energy for the electron–hole pair, respectively.

For **2**, the thermally activated high-energy radiative trapped states dominate the competing processes within the 203–283 K range, while electron–hole pair dissociation dominates above 283 K. The plot of relative fluorescence intensity *versus* temperature was fitted separately for these two temperature intervals, yielding $E_{a1} \approx 41$ meV for **2**; however, no physically meaningful value for E_{a2} could be obtained.

Experimental section

Chemicals and materials

N-Methylpyrrolidine, 1,2-dibromoethane, 1,2-dichloroethane, lead(II) bromide, lead(II) chloride, and DMF (*N*,*N*-dimethyl-

formamide) were used which are chemically pure and commercially available.

Preparation of 1-(2-halo)-1-methylpyrrolidinium halide (X = Br, Cl)

N-Methylpyrrolidine was mixed with 1,2-dibromoethane or 1,2-dichloroethane in a 1 : 1 molar ratio in acetonitrile at ambient temperature and stirred for 4 hours to produce white microcrystalline samples of 1-(2-bromoethyl)-1-methyl-pyrrolidinium bromide or 1-(2-chloroethyl)-1-methyl-pyrrolidinium chloride (abbr. as BrMePyrBr or ClMePyrCl, respectively). The microcrystalline product was filtered and successively washed with ethyl acetate (2 × 20 mL). The white crystalline material was collected, dried in an oven at 60 °C for 1 hour, and stored for further use.

Preparation of 1 and 2

The preparation processes for the two hybrids are similar: BrMePyrBr or ClMePyrCl was mixed with $PbBr_2$ or $PbCl_2$, respectively, in a 1 : 1 molar ratio in a minimal volume of DMF. The mixture was sonicated for 1 hour until a clear solution formed and then filtered *via* suction. The filtrate was evaporated at ambient temperature for over two weeks, yielding white needle-shaped crystals. These crystals were filtered, washed with ethanol, and air-dried for 2 hours. The final products were collected with a yield of ~80% (calculated based on PbX_2). In the IR spectra (Fig. S24), three bands in the range of 3014–2893 cm^{-1} are nearly identical for **1** and **2** and are attributable to the ν(C–H) stretching vibrations of the $XMePyr^+$ (X = Br or Cl) cation. An intense band with two shoulders observed at 1459 cm^{-1} arises from the scissoring vibrations of CH_2 groups. Vibrational bands corresponding to C–Cl and C–Br in the cations were detected at approximately 690 cm^{-1} and 765 cm^{-1}, respectively.[51,52]

Microanalysis calc. for $C_7H_{15}Br_4NPb$ (**1**): C, 13.14%; H, 2.36%; N, 2.19%. Found: C, 13.89%; H, 2.42%; N, 2.26%; Calc. for $C_7H_{15}Cl_4NPb$ (**2**): C, 18.19%; H, 3.27%; N, 3.03%. Found: C, 18.81%; H, 3.09%; N, 3.42%.

Physical measurements

Elemental analyses (C, H, and N) were performed using an Elementar Vario EL III analyzer. Fourier transform infrared (FT-IR) spectra were acquired on a Nicolet 6700 FTIR spectrometer. Powder X-ray diffraction (PXRD) patterns were recorded on a MiniFlex600 diffractometer with Cu Kα radiation (λ = 1.5404 Å) over a 2θ range of 5–50° and a step size of 0.02°. Thermogravimetric (TG) analysis was conducted on an SDT Q600 simultaneous thermal analyzer under a nitrogen flow, using an alumina crucible, with a heating rate of 10 K min^{-1} from room temperature to 1050 K. Differential scanning calorimetry (DSC) was performed on a TA Instruments Q2000 system (version 24.9, Build 121) at a heating/cooling rate of 20 K min^{-1}.

UV-vis diffuse reflectance spectra were recorded in the 200–800 nm wavelength range using a PerkinElmer Lambda 1050 UV-vis spectrophotometer. Photoluminescence emission and excitation spectra, as well as photoluminescence quantum yields (PLQYs), were measured at room temperature using an Edinburgh Instruments FS5-TCSPC transient/steady-state fluorescence spectrometer. Variable temperature photoluminescence emission and excitation spectra were measured using an Edinburgh Instruments FLS1000 transient/steady-state fluorescence spectrometer.

Single crystal X-ray diffraction measurements

Single-crystal X-ray diffraction data were collected on a Rigaku XtaLAB Synergy-DW diffractometer equipped with a graphite monochromator, Mo Kα radiation (λ = 0.71073 Å), and an N-Helix low-temperature attachment. Temperature control was maintained using a laminar flow system and an air dryer. Data reduction was performed using the SAINT program. Empirical absorption correction was applied *via* spherical harmonics, implemented in the SCALE3 ABSPACK scaling algorithm. The structure was solved by the direct method and refined using the full-matrix least-squares technique within the SHELXTL software package.[53] All non-hydrogen atoms were refined anisotropically, while hydrogen atoms were positioned geometrically and constrained to ride on their parent atoms with fixed thermal parameters.

Conclusions

In summary, we have explored the phase transition, crystal structures, thermal expansion behaviors, and fluorescence properties of two newly synthesized isomorphic 1D lead halide hybrids. Both compounds feature edge-sharing PbX_5 (X = Br or Cl) square pyramidal chains and undergo reversible isostructural phase transitions at distinct temperatures, retaining structural isomorphism in both LT and HT phases. These transitions are likely driven by the stereochemically active $6s^2$ lone pair electrons of Pb^{2+} ions. Notably, both materials exhibit uniaxial NTE along the chain direction, attributed to transverse vibrations of chains, and this NTE behavior is intricately coupled with multistate fluorescence, including excitation-dependent dual emission and negative thermal quenching. These findings advance our understanding of structure–property relationships, phase transition dynamics, and NTE mechanisms in lead halide hybrids, offering insightful design strategies for multifunctional optoelectronic materials.

Author contributions

D. S. Shao, W. Ning and X. M. Ren conceived the idea for the manuscript and designed the experiments; G. Yang, W. Ye and Y. Shen developed the synthesis procedures and performed the basic chemical and physical characterization; J. L. Liu and Z. F. Tian assisted in the data analysis; X. M. Ren, W. Ning and D. S. Shao guided the experiments, discussed the data, and led the project; G. Yang wrote the original draft. X. M. Ren, W. Ning, and D. S. Shao reviewed and edited the draft with contributions from all authors.

Conflicts of interest

The authors declare no conflict of interest.

Data availability

CCDC 2467781–2467783 and 2467787 contain the supplementary crystallographic data for this paper.[54a–d]

All data supporting the findings of this study are available within the article and its SI file, or from the authors upon reasonable request. Details of PXRD patterns, crystal structure, TG, DSC, temperature-dependent dielectric permittivity, UV-visible absorption spectra, electronic band structure, optical pictures, VT emission spectra, and IR spectra *etc.* are included in the SI. See DOI: **https://doi.org/10.1039/d5sc05322f**.

Acknowledgements

The authors thank Priority Academic Program Development of Jiangsu Higher Education Institutions, the National Natural Science Foundation of China (grant no. 22073047), the Collaborative Innovation Center of Suzhou Nano Science & Technology, the 111 Project, Joint International Research Laboratory of Carbon-Based Functional Materials and Devices, Suzhou Key Laboratory of Advanced Photonic Materials (grant SZS2023010), and the Gusu Innovation and Entrepreneurship Leading Talent Program (ZXL2023188) for financial support.

Notes and references

1 A. Kojima, K. Teshima, Y. Shirai and T. Miyasaka, *J. Am. Chem. Soc.*, 2009, **131**, 6050–6051.
2 Q. A. Akkerman, A. L. Abdelhady and L. Manna, *J. Phys. Chem. Lett.*, 2018, **9**, 2326–2337.
3 Z. Yuan, C. Zhou, Y. Tian, Y. Shu, J. Messier, J. C. Wang, L. J. van de Burgt, K. Kountouriotis, Y. Xin, E. Holt, K. Schanze, R. Clark, T. Siegrist and B. Ma, *Nat. Commun.*, 2016, **8**, 14051.
4 L. C. An, Z. Y. Li, M. Azeem, W. Li, Y. Qin, F. F. Gao, S. D. Han, G. M. Wang and X. H. Bu, *Angew. Chem., Int. Ed.*, 2024, **63**, e202411298.
5 Z. Wu, C. Ji, L. Li, J. Kong, Z. Sun, S. Zhao, S. Wang, M. Hong and J. Luo, *Angew. Chem., Int. Ed.*, 2018, **57**, 8140–8143.
6 D. Umeyama, L. Leppert, B. A. Connor, M. A. Manumpil, J. B. Neaton and H. I. Karunadasa, *Angew. Chem., Int. Ed.*, 2020, **59**, 19087–19094.
7 H. Y. Zhang, X. J. Song, H. Cheng, Y. L. Zeng, Y. Zhang, P. F. Li, W. Q. Liao and R. G. Xiong, *J. Am. Chem. Soc.*, 2020, **142**, 4604–4608.
8 X. Li, Y. Fu, L. Pedesseau, P. Guo, S. Cuthriell, I. Hadar, J. Even, C. Katan, C. C. Stoumpos, R. D. Schaller, E. Harel and M. G. Kanatzidis, *J. Am. Chem. Soc.*, 2020, **142**, 11486–11496.
9 Y. Xie, J. Morgenstein, K. R. Hansen, H. Hewa Walpitage, C. M. Shirley, P. Amrut, D. Nikiforov, K. Bairley, J. Zhang, N. A. M. S. Caturello, S. Wang, T. Randall, L. Homer, G. Davis, S. Barlow, S. R. Marder, Z. V. Vardeny, J. S. Colton, V. Blum and D. B. Mitzi, *ACS Nano*, 2025, **19**, 12895–12909.
10 S. Yang, W. Niu, A. L. Wang, Z. Fan, B. Chen, C. Tan, Q. Lu and H. Zhang, *Angew. Chem., Int. Ed.*, 2017, **56**, 4252–4255.
11 T. A. S. Doherty, S. Nagane, D. J. Kubicki, Y. K. Jung, D. N. Johnstone, A. N. Iqbal, D. Guo, K. Frohna, M. Daale and S. D. Stranks, *Science*, 2021, **374**, 1598–1605.
12 G. Kim, H. Min, K. S. Lee, D. Y. Lee, S. M. Yoon and S. I. Seok, *Science*, 2020, **370**, 108–112.
13 J. S. Kim, J. M. Heo, G. S. Park, S. J. Woo, C. Cho, H. J. Yun, D. H. Kim, J. Park, S. C. Lee, S. H. Park, E. Yoon, N. C. Greenham and T. W. Lee, *Nature*, 2022, **611**, 688–694.
14 S. Yan, W. Tian, H. Chen, K. Tang, T. Lin, G. Zhong, L. Qiu, X. Pan and W. Wang, *Adv. Opt. Mater.*, 2020, **9**, 2001709.
15 Y. Wang, L. Song, Y. Chen and W. Huang, *ACS Photonics*, 2020, **7**, 10–28.
16 Y. Fan, Q. Chen, Z. Li, T. Zhu, J. Wu, S. You, S. Zhang, J. Luo and C. Ji, *Small*, 2023, **19**, 2303814.
17 C. F. Lin, K. W. Huang, Y. T. Chen, S. L. Hsueh, M. H. Li and P. Chen, *Nanomaterials*, 2023, **13**, 2024.
18 Y. Shi, X. Su, X. Wang and M. Ding, *Polymers*, 2024, **16**, 1568.
19 G. Roma, A. Marronnier and J. Even, *Phys. Rev. Mater.*, 2020, **4**, 092402.
20 T. T. Sha, Y. A. Xiong, Q. Pan, X. G. Chen, X. J. Song, J. Yao, S. R. Miao, Z. Y. Jing, Z. J. Feng, Y. M. You and R. G. Xiong, *Adv. Mater.*, 2019, **31**, 1901843.
21 Y. M. You, W. Q. Liao, D. Zhao, H. Y. Ye, Y. Zhang, Q. H. Zhou, X. H. Niu, J. L. Wang and R. G. Xiong, *Science*, 2017, **357**, 306–309.
22 E. J. Yoo, M. Lyu, J. H. Yun, C. J. Kang, Y. J. Choi and L. Wang, *Adv. Mater.*, 2015, **27**, 6170–6175.
23 Y. Wang, T. Zhang, M. M. Lun, F. L. Zhou, D. W. Fu and Y. Zhang, *Inorg. Chem. Front.*, 2021, **8**, 4230–4238.
24 T. Zhang, C. Chen, W. Y. Zhang, Q. Ye and D. W. Fu, *J. Phys. Chem. C*, 2018, **122**, 20989–20995.
25 M. Keshavarz, M. Ottesen, S. Wiedmann, M. Wharmby, R. Küchler, H. Yuan, E. Debroye, J. A. Steele, J. Martens, N. E. Hussey, M. Bremholm, M. B. J. Roeffaers and J. Hofkens, *Adv. Mater.*, 2019, **31**, 1900521.
26 J. S. Rodríguez Hernández, M. A. P. Gómez, D. S. Abreu, A. Nonato, R. X. da Silva, A. García Fernández, M. A. Señarís Rodríguez, M. Sánchez Andújar, A. P. Ayala and C. W. A. Paschoal, *J. Mater. Chem. C*, 2022, **10**, 17567–17576.
27 K. Dsouza and D. Vashaee, *Mater. Chem. Phys.*, 2023, **299**, 127534.
28 R. A. Saha, A. Halder, D. Fu, M. Itoh, T. Saha Dasgupta and S. Ray, *Inorg. Chem.*, 2021, **60**, 4068–4075.
29 C. Liu, Z. Li, L. Yang, X. Yao, H. Li, X. Liu, Y. Zhao, P. Zhu, T. Cui, C. Sun and Y. Bao, *J. Phys. Chem. C*, 2019, **123**, 30221–30227.
30 S. Maqbool, T. Sheikh, Z. Thekkayil, S. Deswal, R. Boomishankar, A. Nag and P. Mandal, *J. Phys. Chem. C*, 2021, **125**, 22674–22683.
31 L. Zhang, Q. Zeng and K. Wang, *J. Phys. Chem. Lett.*, 2017, **8**, 3752–3758.

32 C. Sun, C. Q. Jing, D. Y. Li, M. H. Dong, M. X. An, Z. H. Zhang, C. Y. Yue, H. Fei and X. W. Lei, *Adv. Sci.*, 2025, **12**, 2412459.
33 C. Y. Chai, Q. K. Zhang, C. Q. Jing, X. B. Han, C. D. Liu, B. D. Liang, C. C. Fan, Z. Chen, X. W. Lei, A. Stroppa, R. O. Agbaoye, G. A. Adebayo, C. F. Zhang and W. Zhang, *Adv. Opt. Mater.*, 2023, **11**, 2201996.
34 L. Shimoni Livny, J. P. Glusker and C. W. Bock, *Inorg. Chem.*, 1998, **37**, 1853–1867.
35 A. Bondi, *J. Phys. Chem.*, 1964, **68**, 441–451.
36 Y. J. Cao, L. Zhou, L. He, P. P. Shi, Q. Ye and D. W. Fu, *Chem.–Eur. J.*, 2020, **26**, 14124–14129.
37 M. M. Lun, F. L. Zhou, D. W. Fu and Q. Ye, *J. Mater. Chem. C*, 2022, **10**, 11371–11378.
38 L. Pan, G. Teri, C. H. Du, Z. J. Xiao, J. Liu, P. Zhuge, P. G. Liu, Q. Q. Jia, Z. X. Zhang, D. W. Fu and Y. Zhang, *Cryst. Growth Des.*, 2025, **25**, 1597–1604.
39 G. Teri, Q. Q. Jia, Q. Guo, Y. Zhang and D. W. Fu, *Sci. China Mater.*, 2023, **66**, 3687–3695.
40 C. Ji, S. Wang, Y. Wang, H. Chen, L. Li, Z. Sun, Y. Sui, S. Wang and J. Luo, *Adv. Funct. Mater.*, 2020, **30**, 1905529.
41 M. J. Cliffe and A. L. Goodwin, *J. Appl. Crystallogr.*, 2012, **45**, 1321–1329.
42 V. N. Bondarev, V. M. Adamyan and V. V. Zavalniuk, *Phys. Rev. B*, 2018, **97**, 035426.
43 P. He, T. Du, K. Zhao, J. Dong, Y. Liang and Q. Zhang, *Adv. Mater.*, 2023, **35**, 2208562.
44 Y. Wang, S. Zhang, B. Zou and R. Zeng, *J. Phys. Chem. C*, 2023, **127**, 7380–7388.
45 J. W. Hu, W. Z. Qiao, J. J. Sun, J. Xu, X. Y. Dong, C. Zhang and S. Q. Zang, *Nano Res.*, 2023, **16**, 7452–7458.
46 Z. Chen, K. Y. Zhang, X. Tong, Y. Liu, C. Hu, S. Liu, Q. Yu, Q. Zhao and W. Huang, *Adv. Funct. Mater.*, 2016, **26**, 4386–4396.
47 X. Y. Dong, Y. Si, J. S. Yang, C. Zhang, Z. Han, P. Luo, Z. Y. Wang, S. Q. Zang and T. C. W. Mak, *Nat. Commun.*, 2020, **11**, 3678.
48 L. Chen, X. Chen, R. Ma, K. Lin, Q. Li, J. P. Lang, C. Liu, K. Kato, L. Huang and X. Xing, *J. Am. Chem. Soc.*, 2022, **144**, 13688–13695.
49 Y. J. Wei, F. Y. Liu, C. C. Chen and I. C. Chen, *Mater. Chem. Phys.*, 2025, **342**, 130992.
50 H. Shibata, *Jpn. J. Appl. Phys.*, 1998, **37**, 550–553.
51 M. Szafran, J. Koput, Z. Dega-Szafran and J. S. Kwiatkowski, *Vib. Spectrosc.*, 2000, **23**, 1–11.
52 L. V. Sennitskaya, B. S. Kikot', O. M. Belokon' and Y. A. Pentin, *J. Appl. Spectrosc.*, 1973, **18**, 750–753.
53 G. M. Sheldrick, *Acta Crystallogr.*, 2015, **71**, 3–8.
54 (*a*) G. Yang, W. Ye, Y. Shen, D.-S. Shao, J.-L. Liu, Z.-F. Tian, W. Ning and X.-M. Ren, CCDC 2467781: Experimental Crystal Structure Determination, 2025, DOI: **10.5517/ccdc.csd.cc2ntxv8**.; (*b*) G. Yang, W. Ye, Y. Shen, D.-S. Shao, J.-L. Liu, Z.-F. Tian, W. Ning and X.-M. Ren, CCDC 2467782: Experimental Crystal Structure Determination, 2025, DOI: **10.5517/ccdc.csd.cc2ntxw9**; (*c*) G. Yang, W. Ye, Y. Shen, D.-S. Shao, J.-L. Liu, Z.-F. Tian, W. Ning and X.-M. Ren, CCDC 2467783: Experimental Crystal Structure Determination, 2025, DOI: **10.5517/ccdc.csd.cc2ntxxb**; (*d*) G. Yang, W. Ye, Y. Shen, D.-S. Shao, J.-L. Liu, Z.-F. Tian, W. Ning and X.-M. Ren, CCDC 2467787: Experimental Crystal Structure Determination, 2025, DOI: **10.5517/ccdc.csd.cc2nty1h**.